Dielectric and Polarimetric Radar Properties of Suspected Surficial Ice Exposures at the Lunar South Pole

Himani, Tanish; Lewis, Kevin; Patterson, G. Wesley; Rivera-Valentín, Edgard G.; Shukla, Shashwat; Dutton, Nicholas

DOI
10.3847/PSJ/adbbe5

Publication date
2025

Document Version
Final published version

Published in
Planetary Science Journal

The Planetary Science Journal, 6:72 (9pp), 2025 March https://doi.org/10.3847/PSJ/adbbe5

Dielectric and Polarimetric Radar Properties of Suspected Surficial Ice Exposures at the Lunar South Pole

Tanish Himani[1], Kevin Lewis[1], G. Wesley Patterson[2], Edgard G. Rivera-Valentín[2], Shashwat Shukla[3], and Nicholas Dutton[2]
[1] Department of Earth & Planetary Sciences, Johns Hopkins University, Baltimore, MD, USA
[2] Johns Hopkins University Applied Physics Laboratory, Laurel, MD, USA
[3] Department of Geoscience and Remote Sensing, Delft University of Technology, Delft, The Netherlands
Received 2024 September 18; revised 2025 February 22; accepted 2025 February 24; published 2025 March 25

Abstract

Various active and passive orbital measurements have provided evidence for surficial water ice within some lunar permanently shadowed regions (PSRs), especially from near-infrared observations by the M^3 instrument. However, radar identification of lunar ice has so far remained ambiguous. Here, we examine the radar-inferred dielectric properties of lunar PSRs and illuminated craters to investigate the potential for ice. We show that the dielectric permittivity of proposed surficial ice-bearing PSRs is lower and has a different distribution than illuminated crater floors of the same diameter range. This difference is confirmed via polarimetric analysis. However, we find that regions with fewer or greater numbers of M^3 detections do not have meaningfully different dielectric properties. The lack of correlation with M^3 detections suggests the differences in radar properties are likely due to a smoother surface at the wavelength scale, perhaps as a consequence of the presence of deeper ice, as suggested by prior studies.

Unified Astronomy Thesaurus concepts: Lunar surface (974); Radar observations (2287); Lunar science (972)

1. Introduction

Permanently shadowed regions (PSRs) at the lunar poles are areas that have remained in shadow over geologic timescales (N. Schörghofer & R. Rufu 2023). Current mapping shows that these PSRs can exist poleward of ±58° latitude over geologic timescales (J. A. McGovern et al. 2013). The presence and stability of water ice in these PSRs has long been considered a possibility due to its low vapor pressure at extremely low temperatures (K. Watson et al. 1961; J. R. Arnold 1979; A. Vasavada 1999). A number of measurements over the past few decades have provided evidence for the existence of buried water ice within PSRs through remote sensing using neutron spectroscopy (W. C. Feldman et al. 1998), radiometry (D. A. Paige et al. 2010), lunar impact experiments (A. Colaprete et al. 2010), and crater geometry (L. Rubanenko et al. 2019). Recently, studies have also shown possible detections of surficial (or surface exposed) water ice at the lunar south pole using a diverse set of remote sensing measurements including neutron spectroscopy (D. J. Lawrence et al. 2011), ultraviolet albedo (P. O. Hayne et al. 2015), Lunar Orbiter Laser Altimeter (LOLA) reflectance (E. A. Fisher et al. 2017), and far-infrared emissivity (E. Sefton-Nash et al. 2019), with some of the strongest evidence coming from near-infrared (NIR) measurements from the M^3 instrument onboard Chandrayaan-1 (S. Li et al. 2018). These NIR measurements were combined with data from other orbiting instruments to create a map of PSRs with the highest likelihood of containing surficial water ice (M. Lemelin et al. 2021). Radar measurements can also provide complimentary observations as radar is sensitive to both wavelength-scale physical characteristics, and electrical properties of the near-surface integrated over the penetration depth (meter scale compared to micron scale for NIR measurements). For example, large water ice deposits on the surfaces of icy moons (D. B. Campbell et al. 1977; S. J. Ostro et al. 1980) and in the PSRs of Mercury (J. K. Harmon & M. A. Slade 1992; M. A. Slade et al. 1992; E. G. Rivera-Valentín et al. 2022) were detected by ground-based measurements of circular polarization ratio (CPR) that exceeded unity and a high radar albedo at high incidence angles.

For the Moon, radar observations have been more ambiguous. Bistatic radar measurements using an Earth-Moon-Clementine geometry found evidence for ice in the form of an opposition surge, which was initially thought to confirm the presence of water ice at the lunar south pole (S. Nozette et al. 1996). However, ground-based measurements of lunar PSRs using the Arecibo observatory did not identify unique CPR enhancements nor high radar albedo (B. A. Campbell et al. 2003; N. J. S. Stacy et al. 1997; D. B. Campbell et al. 2006). Later, orbital radar measurements taken by the Mini-RF instrument onboard the Lunar Reconnaissance Orbiter (LRO) found anomalous craters with high CPR interiors, low CPR exteriors, and high radar albedo (P. D. Spudis et al. 2013). Although the results were initially thought to confirm the existence of water ice, other analyses (W. Fa & Y. Cai 2013; V. R. Eke et al. 2014) showed that the measurements could be caused by wavelength-scale surface features (roughness, high rock abundance, etc.). Recent S-band bistatic measurements of CPR using an Arecibo-Moon-Mini-RF geometry show a strong opposition surge between a 0° and 2° bistatic angle near Cabeus crater that could indicate the presence of blocky, near surface water ice deposits (G. Patterson et al. 2017). This result, though, may be inconsistent with 0° (i.e., monostatic) Mini-RF data of the same region (C. D. Neish et al. 2011). Much of this ambiguity in lunar radar ice detection is because the dominant scattering contributor to CPR varies as a function of incidence

angle (see Figure 10 from W. Fa et al. 2011). Furthermore, even in places known to have thick pure ice deposits like Mercury, CPR is still an unreliable diagnostic compared to newer polarimetric decomposition techniques (see Figures 5(c) and (d) in E. G. Rivera-Valentín et al. 2022).

Overall, the ambiguity of radar measurements of water ice on the Moon indicates that the physical form of ice, its mixing with regolith (K. M. Cannon et al. 2020), or its formation over time (N. Schörghofer & R. Rufu 2023) is different compared to Mercury or the Galilean moons. Nevertheless, radar remains an invaluable tool for water ice detection due to its ability to make measurements in shadowed regions and determine the dielectric properties of the surface and subsurface.

The dielectric constant is a material property described by a dimensionless, complex number. The real part (ϵ_r) describes how much polarization a material experiences in an electric field (such as a radar wave), and the imaginary part describes the absorption of that field in a lossy medium. Early attempts at inverting the lunar surface dielectric constant relied on empirical fits based on Apollo samples (G. Olhoeft & D. Strangway 1975). Recently, a number of inversion methods have been created by fitting scattering laws to measurements from dual-polarized radars like the Dual-frequency Synthetic Aperture Radar onboard Chandraayan-2 (S. S. Bhiravarasu et al. 2021) and hybrid-polarized radars like Mini-RF (B. A. Campbell 2002; S. Shukla et al. 2020; A. Kumar et al. 2022). Specifically, inverting the real part of the dielectric constant of the regolith has shown promise for lunar water ice characterization (N. Liu et al. 2017), especially on the floors of craters (E. Heggy et al. 2020; Y. Gao et al. 2023). Newer approaches include the use of neural networks as a means to solve the inversion problem for larger regions of the lunar surface (S. Shukla et al. 2024), including the poles and PSRs (see Section 2.1). It is important to note that any inversion model of the lunar surface will obtain a derived dielectric constant value, which may not correspond directly with values measured in a laboratory setting. Any given inversion on real radar data is influenced both by the assumptions used to set up the model and by imperfect knowledge of the geophysical parameters of the surface being observed.

In this paper, we use an existing dielectric constant inversion model and radar polarization mosaics of the south pole to quantify population differences between PSRs suspected to contain surficial water ice and non-PSR illuminated crater floors. Section 2 describes the data sets and downselection techniques used for the comparative analysis, and Section 3 describes observed differences within the two crater populations as well as the correlation to other remote sensing data sets.

2. Data Sets and Methods

2.1. Surface Dielectric Constant Inversion Model

The dielectric constant inversion model used in this work is that of S. Shukla et al. (2024). The map of ϵ_r produced therein used existing Mini-RF *S*-band (2.38 GHz, 12.6 cm) controlled south polar mosaics at a resolution of 128 ppd (H. Winters & D. B. Bussey 2008; R. L. Kirk et al. 2013). Compared to both classical curve fits (G. Olhoeft & D. Strangway 1975) that rely on difficult-to-obtain geophysical parameters for the poles (e.g., surface bulk density) or remote sensing approaches that require assumptions on the roughness of the lunar surface (B. A. Campbell 2002), the S. Shukla et al. (2024) model can determine the dielectric constant of more diverse regions of the lunar south pole where our two populations reside (described in Section 2.2). Furthermore, since our goal is to evaluate the presence of surficial water ice, the selected model is useful as it inverts only surface ϵ_r and not the combined surface and subsurface values as previous models have done. While the selected model is in good agreement with Apollo sample drive core measurements of ϵ_r, we also perform an independent check to confirm the relative dielectric constant differences between our two populations using an established polarimetric analysis technique (Section 3.2).

Figure 1 shows all potential surficial-ice-bearing PSRs used in this study, previously mapped by S. Li et al. (2018), overlain on the controlled south polar mosaic of surface ϵ_r from S. Shukla et al. (2024). As is typical for radar measurements, the mosaic shows that ϵ_r increases on radar-facing slopes (e.g., crater walls), which requires us to filter pixels by slope value (described in Section 2.2). The average surface dielectric constant for the mosaic is $\epsilon_r = 2.55$. Note that there are a few data strips located between 120° and 150° west latitude that have image artifacts. Data from these strips were not used in this analysis as neither of our two defined populations were within the image artifact regions. The 1σ per pixel uncertainty of the ϵ_r inversion due to the influence of topography on look direction reported in S. Shukla et al. (2024) is 1.1 for the entire south polar mosaic. This uncertainty is reduced to <0.5 for regions south of 80°S, where the vast majority of our two populations reside. We further reduce this uncertainty by restricting our analysis to low slope regions (Section 2.2) and using measures of central tendency rather than individual pixels (e.g., the median value of all low slope pixels within a given PSR).

2.2. Data Selection

In our analysis, we compare the dielectric constant of two different groups of craters: illuminated craters and potential surficial-ice-hosting craters. For both groups, we focused on simple craters that range from 5 to 25 km in diameter. This size range was chosen because prior studies have shown that the dielectric constant of both Sun-illuminated polar and equatorial crater floors is nearly constant as a function of diameter within this range (E. Heggy et al. 2020; Y. Gao et al. 2023), thus making any deviations easier to detect.

For the illuminated crater group, we use the LROC database of simple craters of size 5–20 km in diameter (R. Z. Povilaitis et al. 2018) and filter these craters to remove those in which a PSR takes up a significant fraction of its area. To do this, we used mapped PSRs $>5\,\mathrm{km}^2$ in area, derived from LOLA and LROC data (E. Mazarico et al. 2011; H. M. Brown et al. 2022). If any of these polygons intersect with a crater in the database, that crater is removed from the data set. We also restrict our analysis to craters poleward of 75°S to match the latitudinal extent of PSR-hosting craters. Finally, we use a LOLA slope map (G. A. Neumann 2009; downsampled to the pixel scale of the Mini-RF dielectric constant mosaic) to include only those pixels on the crater floors that have slope values $<7°$. Slope values below this threshold do not significantly affect radar returns in S-band at the Mini-RF nominal incidence angle (T. W. Thompson et al. 2011). After this filtering, 151 crater floors remain, which we refer to as the illuminated crater floor data and which acts as a control data set.

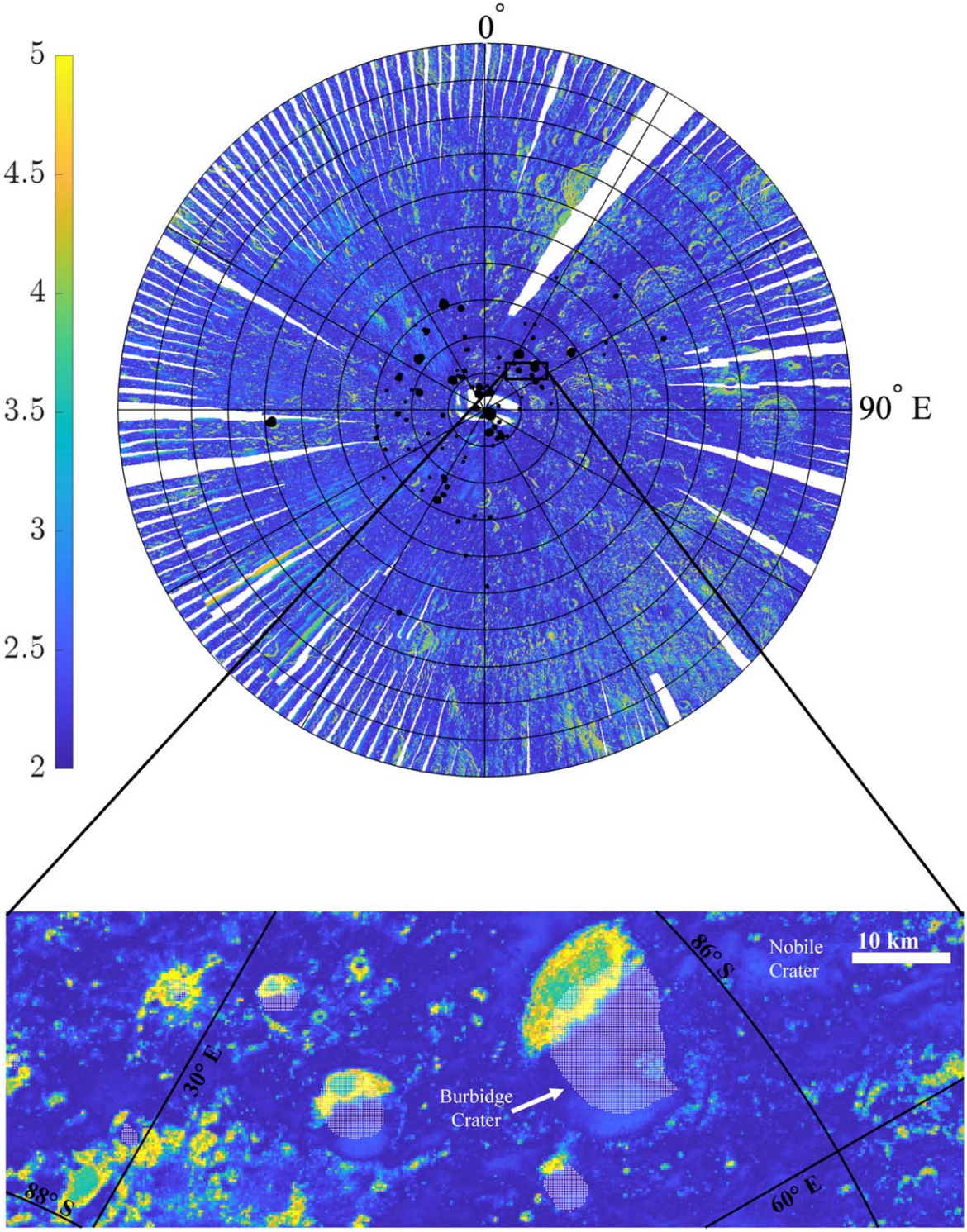

Figure 1. Controlled polar mosaic of real dielectric constant (ϵ_r) for the lunar south pole from 70° to 90° S. Lines of latitude are every 2° and lines of longitude every 30°. PSRs within craters of size 5–25 km are shaded in black. The bottom shows a zoomed version with permanently shadowed areas shaded in white. Figure modified from S. Shukla et al. (2024) to include PSRs.

For the potential surficial-ice-hosting craters, we select permanently shadowed areas suspected to host surficial water ice and that also have modeled ice stability depths between 0 and 2.5 m (a range mostly accessible by Mini-RF's penetration depth). This database was obtained from M. Lemelin et al. (2021), which identifies 169 surficial-water-ice-bearing PSRs, as mapped by the M^3 instrument (S. Li et al. 2018). Their data set includes polygons of the PSRs along with the number of pixels with water ice detections per PSR, both as a total count and on a per-area basis. These values are for each PSR as a whole. We manually cross-referenced this PSR data set with that of S. J. Robbins (2019) to select only those PSRs that have a distinct single host crater with no ambiguous shared PSRs and that fall within a size range of 5–25 km (see Appendix A

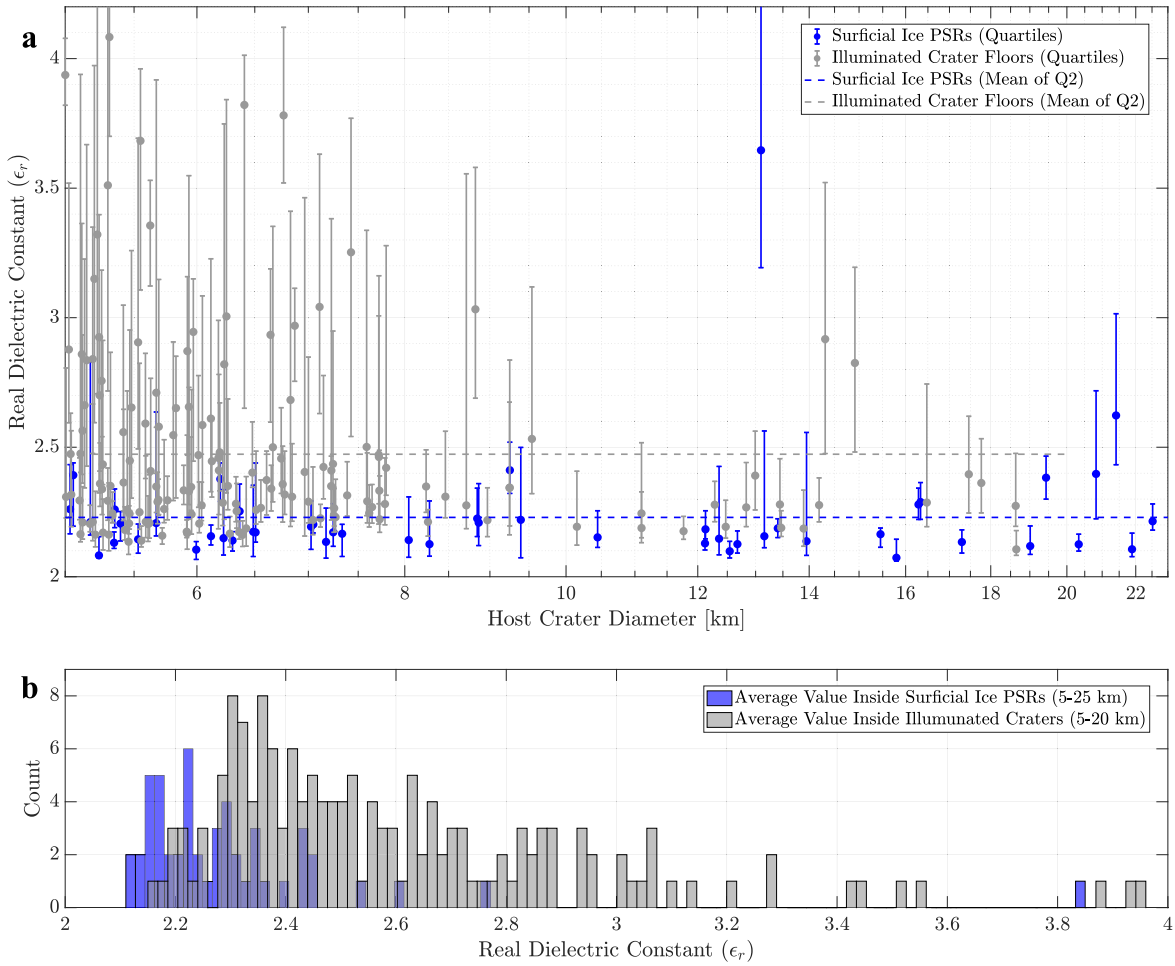

Figure 2. (a) Median real dielectric constant (ϵ_r) within surficial ice PSRs (blue) and illuminated crater floors (gray) as a function of crater diameter. Error bars show the first and third quartiles for each region and the dashed horizontal line denotes the mean of each population's median. (b) Histogram of ϵ_r for both populations described in (a).

for the exact correlated Lemelin PSR IDs and Robbins crater IDs). Doing this reduced the total PSR database from 169 to 51. In order to make appropriate comparisons to the illuminated crater floor data set, we further filtered the PSR database by only including pixels that have a LOLA slope value $<7^\circ$. For brevity, we refer to this data set of potential surficial ice PSRs simply as surficial ice PSRs. We feel this is appropriate since a number of recent studies show that these regions have a high likelihood of containing surface ice (see Section 1).

3. Results and Discussion

3.1. Dielectric Properties of Illuminated Crater Floors versus PSRs

As detailed in Section 2.2, we now compare two populations that represent the highest known likelihood for crater floors lacking water ice (the illuminated crater group) and crater floors containing surface exposed ice (the surficial ice PSR group). The illuminated craters thus act as a direct control for potential surficial-ice-hosting craters. Consistent with prior studies (E. Heggy et al. 2020; Y. Gao et al. 2023), we find no trend in ϵ_r for either population as a function of crater diameter for this diameter range (Figure 2(a)). However, there are two major differences in the distribution of ϵ_r values between the two populations. The first is that the surficial ice PSRs, as a population, have a consistently lower ϵ_r than the illuminated crater floors. Specifically, the surficial ice PSRs have a median average ϵ_r of 2.2, whereas the illuminated crater floors are 2.5. The second major difference is that the surficial ice PSRs have a much lower interquartile spread in their ϵ_r values irrespective of the host crater diameter. There are a few outliers, the most notable being the PSR inside Spudis crater (shown at 13.09 km diameter). This particular PSR has both the highest ϵ_r and the largest interquartile spread in our data set. A histogram of the distribution of the two populations shows that the surficial ice PSR ϵ_r distribution is on average lower than that of the illuminated crater floors (Figure 2(b)). To determine if these two distributions are statistically similar, we perform a Monte Carlo simulation of the two-sample Kolmogorov–Smirnov (K-S) test between these two populations using each individual crater's respective median and standard error of the median values. We find an average p-value <0.01, giving us strong evidence that the populations are not derived from the same underlying distribution. Thus, while there is some overlap in dielectric constant between the two populations, their statistical distributions are meaningfully different. To further illustrate this point, we also performed a similar analysis on PSRs $> 5\,\mathrm{km}^2$ in areas that have zero water ice detections from the M^3 instrument and fall within the same crater diameter and latitude range (see Figure 5 in Appendix B). We find a median average ϵ_r of 2.4, which is closer to the illuminated crater group than the surficial ice PSR group. Thus, simply

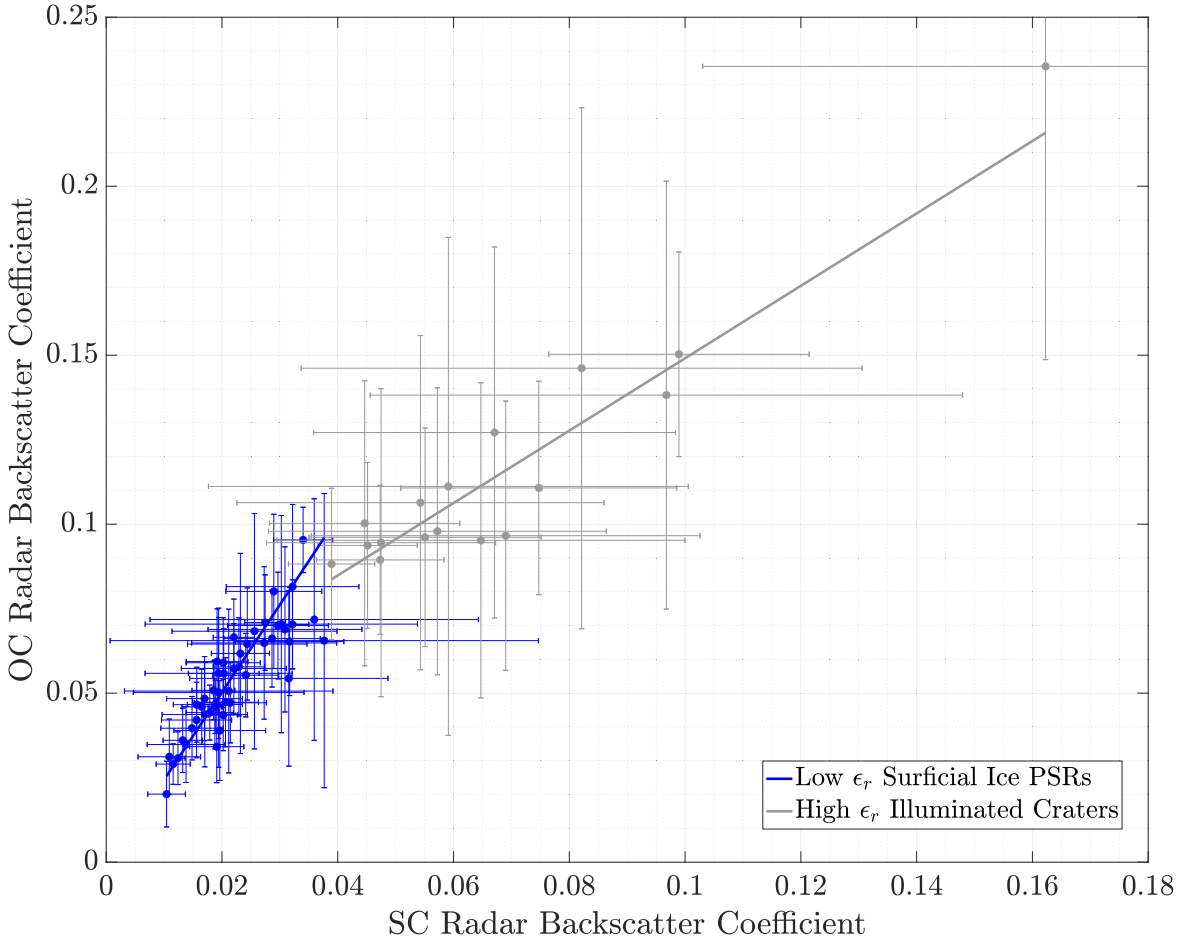

Figure 3. The mean value of SC and OC radar backscatter coefficient for surficial ice PSRs (blue) and illuminated simple crater floors (gray). Both populations are filtered such that the surficial ice PSRs and illuminated crater floors each have an average ϵ_r of less than or greater than 3.0, respectively, as a test of the inversion model. This filtered data contains 48 surficial ice PSRs and 17 illuminated craters. Error bars are 1σ, and trend lines are fit incorporating the 2D errors on each point (D. York et al. 2004). As expected, the two populations have distinct slope and intercept values in SC–OC space.

being in a PSR is not enough to account for the differences in ϵ_r observed between the two populations.

Both model-based and physical factors can decrease the derived ϵ_r of the lunar surface. One important model-based factor in our selected inversion approach is surface roughness, which, in the context of radar remote sensing, is the surface statistical distribution at the wavelength scale (B. A. Campbell 2002). Our selected model, like others, cannot perfectly distinguish between the effects of surface roughness and surface ϵ_r and thus has a tendency to obtain higher dielectric constant values for rougher surfaces (S. Shukla et al. 2024). Recent analysis of surface roughness in ice stability zones has shown that surfaces where ice is stable are smoother than neighboring surfaces where temperatures are too warm for ice (A. N. Deutsch et al. 2021; S. Moon et al. 2021). This was found in ice stability regions with and without M^3 detections (suggesting that buried ice deposits could be playing a role). An influence from terrain smoothing would be consistent both with our results of a lower ϵ_r and with the smaller interquartile spread (due to a more homogeneous surface roughness) for permanently shadowed areas. Other physical factors that can potentially decrease ϵ_r are a reduced boulder population (V. T. Bickel et al. 2021) and the extreme temperatures of lunar regolith within PSRs (M. Kobayashi et al. 2023). Depending on its form, surficial water ice can also play a role in decreasing the ϵ_r of crater floors. Pure water ice at lunar PSR temperatures is expected to have a $\epsilon_r = 3.15$ (see Table 1 in W. Fa et al. 2011, and references therein), whereas mixtures of regolith, ice, and vacuum can have a $\epsilon_r \leqslant 2$ depending on the porosity and volume percentage of ice (W. Fa et al. 2011; E. Heggy et al. 2019). While thick deposits of pure water ice likely cannot be uniquely characterized by measuring ϵ_r, the overall decrease in ϵ_r compared to illuminated floors shows that these PSRs are inconsistent with the presence of thick pure water ice on the surface. This is in agreement with prior observations (see Section 1) that rule out these types of deposits in lunar PSRs. However, our results could be consistent with higher porosity or the presence of porous regolith/ice mixtures that can cause a decrease in the average ϵ_r within each PSR.

3.2. Polarimetric Properties of Illuminated Crater Floors versus PSRs

In order to verify that our chosen inversion model is revealing true differences in real dielectric constant between our two populations, we implemented an independent check on the inversion results. This approach is based on polarimetric analysis of each region's distribution of the same sense circular (SC; $\hat{\sigma}_{SC}$) and opposite sense circular (OC; $\hat{\sigma}_{OC}$) polarization values (A. K. Virkki & S. S. Bhiravarasu 2019; E. G. Rivera-Valentín et al. 2022; A. K. Virkki et al. 2023). The $\hat{\sigma}_{SC}$ and $\hat{\sigma}_{OC}$ values were derived from Mini-RF S-band controlled polar

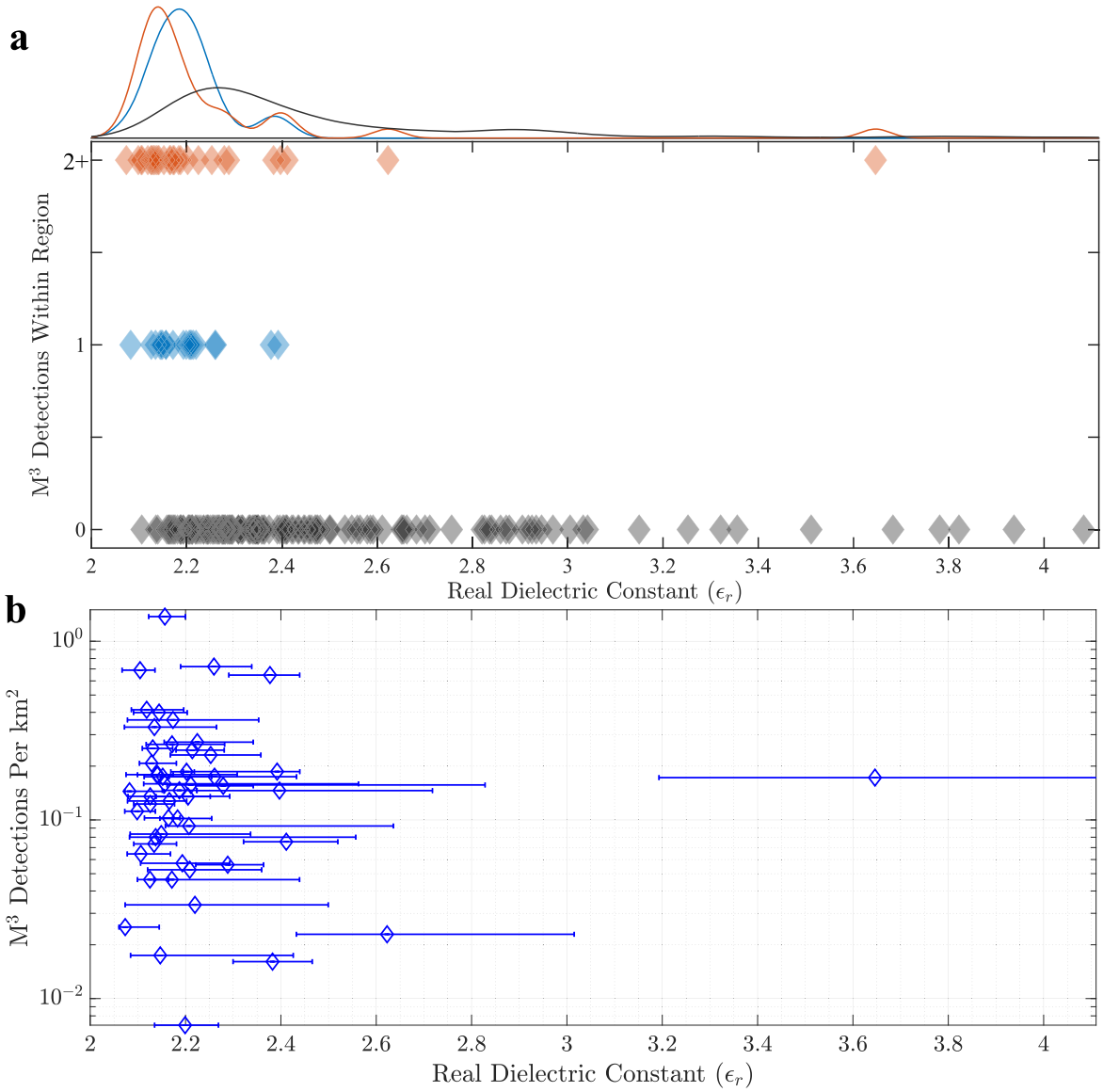

Figure 4. (a) Scatter-histogram plot: the bottom is a scatterplot showing illuminated crater floors with no M^3 detections (gray), surficial ice PSRs with one M^3 detections (blue), and surficial ice PSRs with two or more M^3 detections (orange) as a function of real dielectric constant (ϵ_r). Above is a kernel density estimate of the histogram of each of the three populations. (b) M^3 detections per km^2 versus ϵ_r for surficial ice PSRs. The ϵ_r values are the median and interquartile range within each region.

mosaics of the full Stokes vector (R. L. Kirk et al. 2013) using the procedure described in M. Reid (2010). In an $\hat{\sigma}_{SC}-\hat{\sigma}_{OC}$ space, differences in the intercept of a best-fit line through the data represent relative differences in the dielectric constant. Furthermore, the differences in slope of a best-fit line are due to either particle size distribution or morphology (A. K. Virkki & S. S. Bhiravarasu 2019). To accentuate differences, we segment the two populations using a threshold of $\epsilon_r = 3.0$ so that only surficial ice PSRs with an average ϵ_r below this value and only illuminated crater floors with an average ϵ_r above this value are selected. This threshold is a simple way to ensure the polarimetric analysis is applied to two distinct ϵ_r populations rather than comparing overlapping ϵ_r distributions. Further data reduction was done to remove outliers in both data sets with large errors (i.e., 1σ errors that fall below zero $\hat{\sigma}_{SC}$ or $\hat{\sigma}_{OC}$). The intercept values of the two populations are 0.001 ± 0.009 for the surficial ice PSRs and 0.042 ± 0.030 for the illuminated crater floors (Figure 3). From A. K. Virkki & S. S. Bhiravarasu (2019), this implies that the inversion is producing, at minimum, relative differences in dielectric constant between the two segmented populations. This is consistent with the results from the full data set shown in Section 3.1 and gives confidence that the differences in surface ϵ_r between surficial ice PSRs and illuminated crater floors are physical and not a result of bias within the inversion process. Slope values of the two segmented populations are 2.6 ± 0.4 for the surficial ice PSRs and 1.1 ± 0.5 for the illuminated crater floors. The larger slope value for the surficial ice PSRs may imply either a particle size distribution with fewer wavelength-scale particles (e.g., discrete rocks or cobble) or a particle morphology that is more rounded than those within the illuminated crater floors. Fewer wavelength-scale particles could be caused by a decrease in rock abundance within PSRs and more rounded particle morphologies could be caused be due to ice condensation on regolith particles, similar to how

freeze–thaw cycles can affect the geometry of terrestrial soil particles (Q. Liu et al. 2023).

3.3. Comparison to M^3 Infrared Ice Detections

The data set of surficial-ice-bearing PSRs reported in M. Lemelin et al. (2021) includes the number of M^3 pixels within each PSR that show a positive detection of surficial water ice as determined by S. Li et al. (2018). We now segment the surficial ice PSRs into two categories: a single M^3 detection and multiple M^3 detections (Figure 4(a)). The vast majority of the multiple detections are between 2 and 10 M^3 pixels, with two notable outliers: Shackleton ($N = 34$), and an unnamed crater north of Shackleton and east of Sverdrup ($N = 36$). All illuminated crater floors have no M^3 water ice detections. For visualization purposes, Figure 4(a) also shows a kernel density estimate (Gaussian kernel with bandwidth of 0.0732) of the distribution of M^3 detections of each category defined above as a function of ϵ_r. From this, we can see that the surficial ice PSRs have a ϵ_r distribution that is clustered on the lower end regardless of the number of M^3 detections. In contrast, the illuminated crater floor regions have a broader distribution of ϵ_r values, with the majority between $\epsilon_r = 2.2$ and 3. The peak of the distribution for single and multiple M^3 detection PSRs is $\epsilon_r = 2.18$ and 2.14, respectively, whereas the peak for the illuminated crater floors is $\epsilon_r = 2.26$. Regions with a single detection versus multiple detections do not seem to have a meaningfully different distribution of ϵ_r. We confirm this by running another Monte Carlo simulation of two-sample K-S tests with both the single and multiple M^3 detection regions and find an average p-value >0.5, indicating insufficient evidence that these two populations are derived from different distributions.

These results show that the distribution of ϵ_r values can be used as an independent check on future detections of porous water ice on the surface relative to NIR spectroscopy. However, if a greater number of M^3 detections correspond to a greater mass/volume percentage of ice, our analysis of ϵ_r is not sensitive enough to discern differences between lower and higher concentrations of ice. Furthermore, we find no increase in M^3 detections on a per-area basis for surficial ice PSRs with lower average ϵ_r (as shown in Figure 4(b)), which would be expected if the lower ϵ_r was exclusively due to the presence of porous ice mixtures on the surface.

4. Conclusions

We applied an existing surface real dielectric constant inversion model to two populations of simple crater floors of size range 5–25 km in diameter. The first are crater floors containing PSRs that are suspected to contain surficial water ice as measured by the M^3 instrument (i.e., surficial ice PSRs), and the second are floors of illuminated craters. We find that the median surface ϵ_r within these PSRs is, on average, lower than that of illuminated crater floors and generally has a smaller interquartile spread. Polarimetric analysis was used as an independent check to validate the inversion results, showing that not only is ϵ_r for surficial ice PSRs lower (consistent with our prior analysis) but also that these regions likely have a different scatterer size distribution or morphology. Looking at the number of M^3 water ice detections within each region, we find that there is no difference in the distribution of ϵ_r between those surficial ice PSRs that contain a single M^3 detection compared with those that contain multiple detections. Perhaps the increase in water ice concentration going from a single detection to multiple detections is still not sufficient to be within the sensitivity of our analysis. Likewise, the number of M^3 detections per square kilometer within these PSRs does not correlate with the median ϵ_r within each respective region. However, we note that the size of M^3 pixels is much larger than that of Mini-RF, so this lack of correlation may not apply to many of the smaller craters, which only contain one or two pixels. Thus, while the difference in ϵ_r for our two populations of crater floors could be consistent with the presence of porous ice mixtures, a smaller interquartile spread and lack of correlation to M^3 pixel detections (both in total pixels and on a per-area basis) suggests that a smoother surface may be a more apt explanation for the lower ϵ_r observed within these PSRs. The smoother surface could be a secondary effect of the presence of water ice either on the surface or subsurface. Future work in this area would require a full treatment of CPR modeling (accounting for both the presence of surface ice and wavelength scale near-surface roughness) to determine whether radar polarization supports a smoother surface within these surficial ice PSRs. Still, radar data can play a complementary role to the detection and characterization of surficial ice deposits from NIR instruments such as M^3. Since each type of measurement is sensitive to different physical properties of water ice, they help serve as independent checks on each other.

Acknowledgments

Dielectric constant mosaics were obtained from S. Shukla et al. (2024). Data used to generate figures are available on Zenodo at doi:10.5281/zenodo.13760875. This research was partially supported by NASA through the LRO project, Contract No. NNN16AA05T. Funding for the first author is provided by the Johns Hopkins University Applied Physics Laboratory Graduate Fellowship. We are also grateful to the Mini-RF team for supporting this work and for the collection of the data. The authors thank the two anonymous reviewers and the data editor whose feedback significantly improved the quality of this manuscript.

Software: Linear Regression with Errors in X and Y (T. Wiens 2023).

Appendix A
Associated Craters and PSRs

Table 1 shows all PSR IDs and associated crater IDs used in our analysis.

Table 1
PSRs (Lemelin FID) and Associated Crater (Robbins ID)

PSR (Lemelin FID)	Crater (Robbins ID)
14	10-2-000451
16	10-2-000470
19	10-1-072826
22	10-2-012400
24	10-1-000708
26	10-1-000710
27	10-2-002449
28	10-1-079428
29	10-2-002109
31	10-2-001254
33	10-1-079219
34	10-2-001268
35	10-1-082923
36	10-1-083166
39	10-2-001298
40	10-1-083342
41	10-1-083146
42	10-1-000792
43	10-2-001272
44	10-2-001365
50	10-1-000791
51	10-2-001391
53	10-2-001392
55	10-2-004380
56	10-2-004493
58	10-2-001406
59	10-2-001352
60	10-2-001403
61	10-2-001372
63	10-2-001354
64	10-2-001407
67	10-2-001494
68	10-1-001314
70	10-2-000665
72	10-2-001488
74	10-2-001477
75	10-2-001483
76	10-2-001451
77	10-2-001520
78	10-2-000694
79	10-1-088585
81	10-1-000851
83	10-1-001313
84	10-2-002046
87	10-2-001594
93	10-1-090401
95	10-2-001624
99	10-2-006663

Table 1
(Continued)

PSR (Lemelin FID)	Crater (Robbins ID)
100	10-2-001565
104	10-2-001739
106	10-2-002050
107	10-2-001709
108	10-1-090536
111	10-2-001736
113	10-1-000880
114	10-2-012927
116	10-1-000875
119	10-2-001726
120	10-2-001695
121	10-1-094454
122	10-1-094341
123	10-2-001853
124	10-1-094222
125	10-2-001809
129	10-2-001823
131	10-2-009139
132	10-2-001944
133	10-1-094318
135	10-1-094272
136	10-2-001771
137	10-2-001906
138	10-2-001903
142	10-2-001960
143	10-1-000918
144	10-2-013204
146	10-1-099087
147	10-2-001978
149	10-1-102381
151	10-1-000919
152	10-1-000935
158	10-2-013474
159	10-2-013479
160	10-2-013471
163	10-1-113145
165	10-2-014104
168	10-2-014239

Appendix B
PSRs without Surficial Ice Detections

Figure 5 shows the dielectric constant as a function of host crater diameter for PSRs > 5 km^2 that have zero water ice detections from the M^3 instrument.

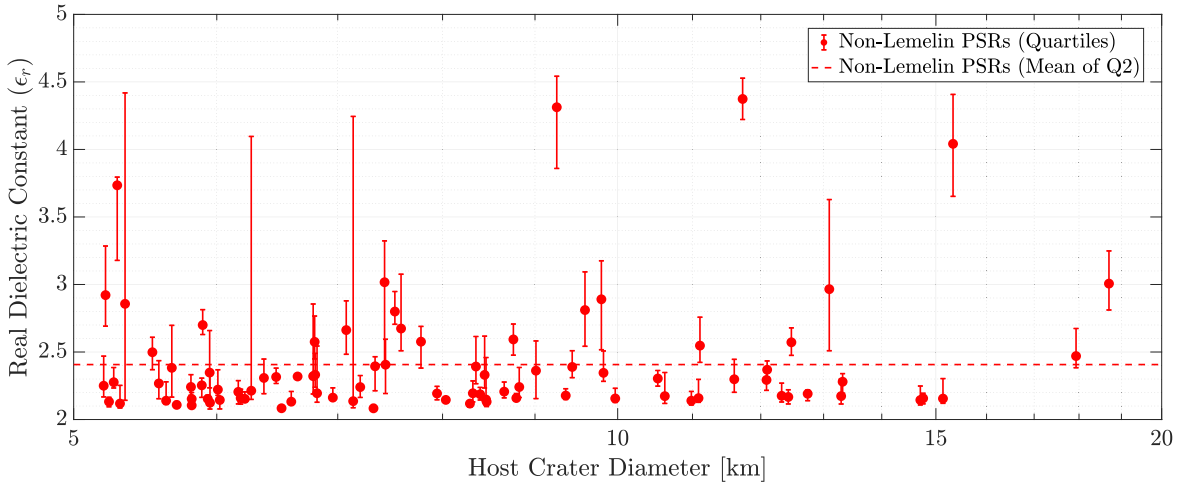

Figure 5. Median real dielectric constant (ϵ_r) within PSRs lacking surficial water ice detections as a function of crater diameter. Error bars show the first and third quartiles for each region and the dashed horizontal line denotes the mean of the population's median.

ORCID iDs

Tanish Himani https://orcid.org/0000-0003-3029-5631
Kevin Lewis https://orcid.org/0000-0003-3412-803X
G. Wesley Patterson https://orcid.org/0000-0003-4787-3899
Edgard G. Rivera-Valentín https://orcid.org/0000-0002-4042-003X
Shashwat Shukla https://orcid.org/0000-0003-4537-2708
Nicholas Dutton https://orcid.org/0009-0004-0837-8160

References

Arnold, J. R. 1979, JGR, 84, 5659
Bhiravarasu, S. S., Chakraborty, T., Putrevu, D., et al. 2021, PSJ, 2, 134
Bickel, V. T., Moseley, B., Lopez-Francos, I., & Shirley, M. 2021, NatCo, 12, 5607
Brown, H. M., Boyd, A. K., Sonke, A., et al. 2022, Lunar Reconnaissance Orbiter Camera Permanently Shadowed Region Images: Updates to PSR Atlas and PSR Mosaics, in Lunar Polar Volatiles Conf. 2703 (Boulder, CO: Lunar and Planetary Institute), 5033
Campbell, B. A. 2002, Radar Remote Sensing of Planetary Surfaces (Cambridge: Cambridge Univ. Press)
Campbell, B. A., Campbell, D. B., Chandler, J. F., et al. 2003, Natur, 426, 137
Campbell, D. B., Campbell, B. A., Carter, L. M., Margot, J.-L., & Stacy, N. J. S. 2006, Natur, 443, 835
Campbell, D. B., Chandler, J. F., Pettengill, G. H., & Shapiro, I. I. 1977, Sci, 196, 650
Cannon, K. M., Deutsch, A. N., Head, J. W., & Britt, D. T. 2020, GeoRL, 47, e2020GL088920
Colaprete, A., Schultz, P., Heldmann, J., et al. 2010, Sci, 330, 463
Deutsch, A. N., Heldmann, J. L., Colaprete, A., Cannon, K. M., & Elphic, R. C. 2021, PSJ, 2, 213
Eke, V. R., Bartram, S. A., Lane, D. A., Smith, D., & Teodoro, L. F. 2014, Icar, 241, 66
Fa, W., & Cai, Y. 2013, JGRE, 118, 1582
Fa, W., Wieczorek, M. A., & Heggy, E. 2011, JGR, 116, E03005
Feldman, W. C., Maurice, S., Binder, A. B., et al. 1998, Sci, 281, 1496
Fisher, E. A., Lucey, P. G., Lemelin, M., et al. 2017, Icar, 292, 74
Gao, Y., Dang, Y., Lu, P., et al. 2023, JPRS, 197, 56
Harmon, J. K., & Slade, M. A. 1992, Sci, 258, 640
Hayne, P. O., Hendrix, A., Sefton-Nash, E., et al. 2015, Icar, 255, 58
Heggy, E., Palmer, E., Thompson, T., Thomson, B., & Patterson, G. 2020, E&PSL, 541, 116274
Heggy, E., Palmer, E. M., Hérique, A., Kofman, W., & El-Maarry, M. R. 2019, MNRAS, 489, 1667
Kirk, R. L., Becker, T. L., Shinaman, J., et al. 2013, A Radargrammetric Control Network and Controlled Mini-RF Mosaics of the Moon's North Pole...At Last!, LPSC, 44, 2920
Kobayashi, M., Miyamoto, H., Pál, B. D., Niihara, T., & Takemura, T. 2023, EP&S, 75, 8
Kumar, A., Kochar, I. M., Pandey, D. K., et al. 2022, ITGRS, 60, 3103383
Lawrence, D. J., Hurley, D. M., Feldman, W. C., et al. 2011, JGRE, 116, E01002
Lemelin, M., Li, S., Mazarico, E., et al. 2021, PSJ, 2, 103
Li, S., Lucey, P. G., Milliken, R. E., et al. 2018, PNAS, 115, 8907
Liu, N., Ye, H., & Jin, Y.-Q. 2017, IGRSL, 14, 1444
Liu, Q., Zhang, Z., Zhai, J., et al. 2023, EngGe, 320, 107133
Mazarico, E., Neumann, G. A., Smith, D. E., Zuber, M. T., & Torrence, M. H. 2011, Icar, 211, 1066
McGovern, J. A., Bussey, D. B., Greenhagen, B. T., et al. 2013, Icar, 223, 566
Moon, S., Paige, D. A., Siegler, M. A., & Russell, P. S. 2021, GeoRL, 48, e2020GL090780
Neish, C. D., Bussey, D. B. J., Spudis, P., et al. 2011, JGRE, 116, E01005
Neumann, G. A. 2009, Lunar Orbiter Laser Altimeter Raw Data Set, LRO-L-LOLA-4-GDR-V1.0, NASA Planetary Data System, doi:10.17189/1520642
Nozette, S., Lichtenberg, C. L., Spudis, P., et al. 1996, Sci, 274, 1495
Olhoeft, G., & Strangway, D. 1975, E&PSL, 24, 394
Ostro, S. J., Campbell, D. B., Pettengill, G. H., & Shapiro, I. I. 1980, Icar, 44, 431
Paige, D. A., Siegler, M. A., Zhang, J. A., et al. 2010, Sci, 330, 479
Patterson, G., Stickle, A., Turner, F., et al. 2017, Icar, 283, 2
Povilaitis, R. Z., Robinson, M. S., van der Bogert, C. H., et al. 2018, P&SS, 162, 41
Reid, M. 2010, PDS Data Product Software Interface Specification (SIS) For Mini-RF Advanced Technologies (Washington, DC: NASA)
Rivera-Valentín, E. G., Meyer, H. M., Taylor, P. A., et al. 2022, PSJ, 3, 62
Robbins, S. J. 2019, JGRE, 124, 871
Rubanenko, L., Venkatraman, J., & Paige, D. A. 2019, NatGe, 12, 597
Schörghofer, N., & Rufu, R. 2023, SciA, 9, eadh4302
Sefton-Nash, E., Williams, J.-P., Greenhagen, B., et al. 2019, Icar, 332, 1
Shukla, S., Patterson, G. W., Maiti, A., Kumar, S., & Dutton, N. 2024, RemS, 16, 3208
Shukla, S., Tolpekin, V., Kumar, S., & Stein, A. 2020, RemS, 12, 3350
Slade, M. A., Butler, B. J., & Muhleman, D. O. 1992, Sci, 258, 635
Spudis, P. D., Bussey, D. B. J., Baloga, S. M., et al. 2013, JGRE, 118, 2016
Stacy, N. J. S., Campbell, D. B., & Ford, P. G. 1997, Sci, 276, 1527
Thompson, T. W., Ustinov, E. A., & Heggy, E. 2011, JGR, 116, E01006
Vasavada, A. 1999, Icar, 141, 179
Virkki, A. K., & Bhiravarasu, S. S. 2019, JGRE, 124, 3025
Virkki, A. K., Neish, C. D., Rivera-Valentín, E. G., et al. 2023, RemS, 15, 5605
Watson, K., Murray, B. C., & Brown, H. 1961, JGR, 66, 3033
Wiens, T. 2023, Linear Regression with Errors in X and Y, https://www.mathworks.com/matlabcentral/fileexchange/26586-linear-regression-with-errors-in-x-and-y
Winters, H., & Bussey, D. B. 2008, LRO Mini-RF Calibrated Level 2 Data Set v1.0, LRO-L-MRFLRO-5-CDR-MAP-V1.0, NASA Planetary Data System, doi:10.17189/1520649
York, D., Evensen, N. M., Martinez, M. L., & De Basabe Delgado, J. 2004, AmJPh, 72, 367